

In Situ Nano-thermomechanical Experiment Reveals Brittle to Ductile Transition in Silicon Nanowires

Guangming Cheng,[†] Yin Zhang,[‡] Tzu-Hsuan Chang,[†] Qunfeng Liu,^{‡,†} Lin Chen,[§] Wei D. Lu,[§] Ting Zhu,^{*,‡} and Yong Zhu^{*,†}

[†]Department of Mechanical and Aerospace Engineering, North Carolina State University, Raleigh, North Carolina 27695, United States

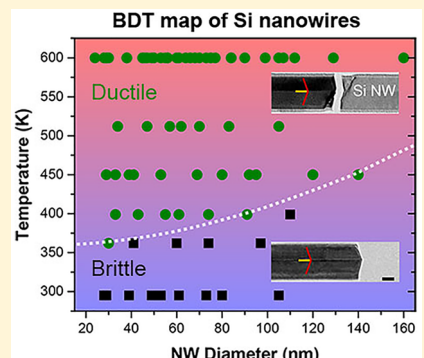
[‡]Woodruff School of Mechanical Engineering, Georgia Institute of Technology, Atlanta, Georgia 30332, United States

[§]Department of Electric Engineering and Computer Science, University of Michigan, Ann Arbor, Michigan 48109, United States

^{*}School of Architecture and Civil Engineering, Xi'an University of Science and Technology, Xi'an 710054, China

Supporting Information

ABSTRACT: Silicon (Si) nanostructures are widely used in microelectronics and nanotechnology. Brittle to ductile transition in nanoscale Si is of great scientific and technological interest but this phenomenon and its underlying mechanism remain elusive. By conducting in situ temperature-controlled nanomechanical testing inside a transmission electron microscope (TEM), here we show that the crystalline Si nanowires under tension are brittle at room temperature but exhibit ductile behavior with dislocation-mediated plasticity at elevated temperatures. We find that reducing the nanowire diameter promotes the dislocation-mediated responses, as shown by 78 Si nanowires tested between room temperature and 600 K. In situ high-resolution TEM imaging and atomistic reaction pathway modeling reveal that the unconventional $1/2\langle 110 \rangle\{001\}$ dislocations become highly active with increasing temperature and thus play a critical role in the formation of deformation bands, leading to transition from brittle fracture to dislocation-mediated failure in Si nanowires at elevated temperatures. This study provides quantitative characterization and mechanistic insight for the brittle to ductile transition in Si nanostructures.



KEYWORDS: Brittle to ductile transition, dislocation, plasticity, silicon nanowire, in situ TEM

Silicon nanostructures have been used extensively in modern microelectronics. The ever-increasing integration density in microelectronic chips inevitably leads to a marked temperature rise of Si nanostructures, which are required to withstand large thermal stresses for maintaining their proper functions. Si nanostructures are also the building blocks for many novel nanotechnology applications, including energy harvesting and storage, flexible and stretchable electronics, sensors, and nanoelectromechanical systems.^{1–5} The reliability concerns of these applications call for a fundamental understanding of the mechanical behavior of Si nanostructures at elevated temperatures.

Brittle to ductile transition (BDT) in Si has been of great scientific and technological interest for a long time.⁶ For bulk Si crystals, BDT was observed in the temperature range from 0.32 to 0.70 T_m (with T_m being the Si melting temperature of 1414 °C) under different loading conditions such as tension, indentation, compression, and bending.^{7–15} The BDT phenomenon was understood in terms of the change of dislocation nucleation rate or dislocation mobility with loading rate and temperature.^{16–19} For nanoscale Si, experimental studies on BDT have been scarce. Evidence of BDT at room temperature (RT) was found during indentation/compression of Si nano-

particles²⁰ and nanopillars,^{8,21} as well as during tension^{22–24} or bending^{25–28} of Si nanowires (NWs), whereas brittle fracture was observed in Si NWs under tension at RT.^{22,29–33} The BDT in nanoscale Si at RT was attributed to either dislocation plasticity under large hydrostatic stresses or amorphization induced by high tensile stresses. However, these results remain controversial, largely due to a lack of nanomechanical testing over a range of temperatures, which is essential to establishing the BDT phenomenology and further elucidating the BDT mechanisms in nanoscale Si. Hence, there is a critical need for the in situ temperature-controlled quantitative nanomechanical characterization of BDT in nanoscale Si, especially under tensile loading. Although significant advances have been made for in situ mechanical testing of nanostructures at RT,^{34–36} the nanomechanical testing at elevated temperatures remains a challenge.

Here we report the in situ tensile testing of single crystal Si NWs in the temperature range of RT to 600 K. We employ a newly developed microelectromechanical system (MEMS) for

Received: May 1, 2019

Revised: July 12, 2019

Published: July 17, 2019

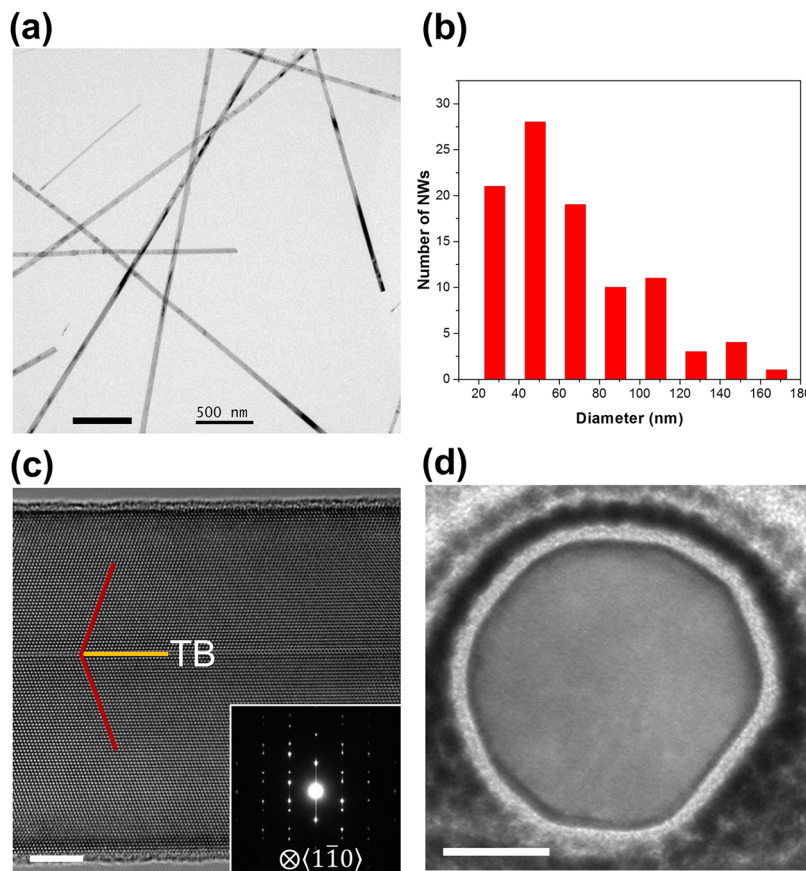


Figure 1. Microstructure characterization of Si NWs. (a) Low-magnification TEM image of Si NWs. Scale bar, 500 nm. (b) Size distribution of $\langle 112 \rangle$ -oriented Si NWs with diameters ranging from 24 to 160 nm (97 NWs examined). (c) HRTEM image of a $\langle 112 \rangle$ -oriented Si NW with a central twin boundary running parallel to the axial direction. The inset shows the corresponding selected area electron diffraction (SAED) pattern. Scale bar, 5 nm. (d) TEM image showing the typical cross section of $\langle 112 \rangle$ -oriented Si NWs. Scale bar, 20 nm.

conducting the nano-thermomechanical testing inside a transmission electron microscope (TEM) (see [Materials and Methods](#)). This platform allows stress-strain measurement with simultaneous TEM imaging of atomic-scale deformation at different temperatures.^{37–39} An on-chip heater is built into the MEMS-based platform, allowing the controlled heating of the specimen. Our results show that the Si NWs tested at elevated temperatures exhibit pronounced dislocation-mediated plastic deformation followed by fracture, which stands in contrast to brittle cleavage fracture in the Si NWs tested at RT. Our in situ high-resolution TEM imaging and atomistic reaction pathway modeling^{40,41} reveal the critical role of unconventional $1/2\langle 110 \rangle\{001\}$ dislocations in the plastic deformation of Si NWs at elevated temperatures. We tested 78 Si NWs to systematically investigate the effects of size and temperature on dislocation-mediated plasticity and fracture.

Results. Single crystal Si NWs were synthesized by chemical evaporation deposition through the vapor–liquid–solid mechanism. These NWs grow uniformly in the axial direction ([Figure 1a](#)) and have diameters ranging from 24 to 160 nm ([Figure 1b](#)). All Si NWs used for mechanical testing are $\langle 112 \rangle$ -oriented and have a central $\{111\}$ twin boundary running parallel to the axial direction of the NW ([Figure 1c](#)). [Figure 1d](#) shows a typical cross section of the $\langle 112 \rangle$ -oriented NW.

In situ TEM tensile testing of individual Si NWs was performed at temperatures ranging from 295 to 600 K. In [Figure 2](#), we compare the brittle response at RT (295 K) with the moderate ductile behavior at 600 K for Si NWs with similar

diameters. [Figure 2a](#) shows the stress–strain curve of a Si NW with a diameter of 61 nm at 295 K. This NW initially exhibited a linear elastic response. As the tensile strain increased to 7.4% and the corresponding tensile stress to 11.5 GPa, brittle fracture occurred. The inset in [Figure 2a](#) shows a TEM image of the sharp $\{111\}$ cleavage surfaces (see more details in [Figures S2 and S3](#) and [Movie 1](#)), which are known to have the lowest surface energy and also typically observed during brittle fracture of bulk Si crystals.⁴² The two fracture surfaces in the upper and lower twin variants are symmetric and tilted at $\sim 70^\circ$ with respect to the axial direction.

In contrast, the Si NW with a diameter of 66 nm at 600 K exhibited moderate ductile behavior. As shown in [Figure 2b](#), the tensile stress–strain curve was initially linear and became slightly nonlinear with increasing stress until the maximum stress of 5.8 GPa was reached at the critical strain of 4.0%. Subsequently, the stress decreased with increasing strain, and this softening response continued until fracture occurred at the strain of 4.7%. The inset in [Figure 2b](#) shows the TEM image of fracture surfaces, which exhibit the features of ductile failure such as localized necking, deformation bands and rough fracture planes ([Figure S4](#) and [Movie 2](#)). [Figure 2c](#) shows the TEM snapshots during in situ tensile testing at 600 K, and the corresponding stress/strain for each snapshot is marked in [Figure 2b](#). It is seen that the maximum stress and ensuing softening response can be associated with surface nucleation and migration of dislocations as well as dislocation interactions with the twin boundary, as marked by blue arrows in [Figure 2cii–iv](#).

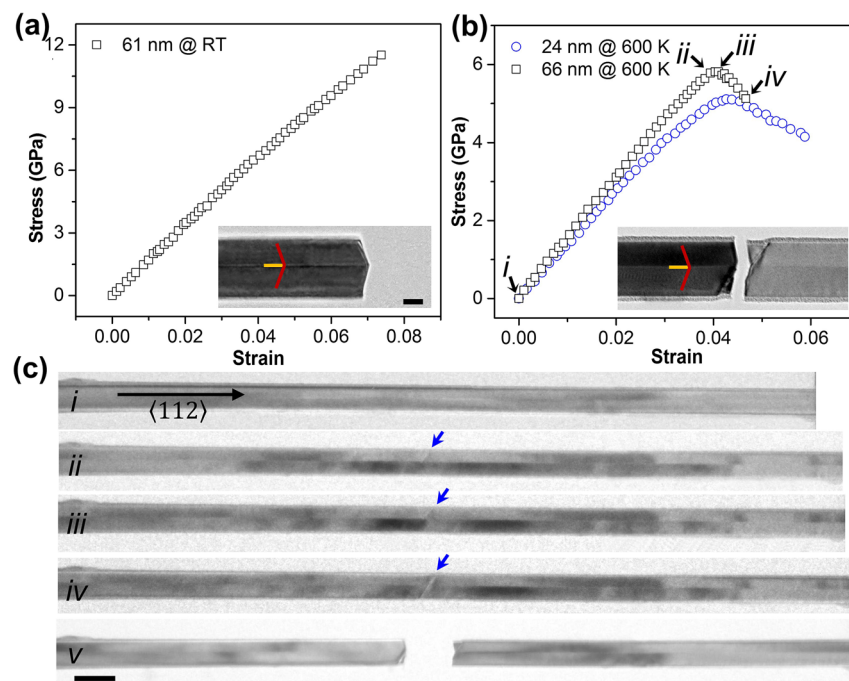


Figure 2. In situ MEMS-based measurement and TEM observation of mechanical behavior of individual Si NWs under uniaxial tension at room and elevated temperatures. (a,b) Stress–strain curves of Si NWs tested at 295 and 600 K, respectively. Insets in (a,b) are the corresponding fracture morphologies of the tested NWs with diameters of 61 and 66 nm, respectively. Scale bar, 20 nm. (c) Snapshots of microstructure evolution corresponding to (b). Each snapshot corresponds to a data point marked in (b). Blue arrows indicate the dislocation activities, including (ii) surface nucleation, (iii) obstruction by twin boundary and (iv) slip transmission across twin boundary. Scale bar, 100 nm.

These continued dislocation processes resulted in large plastic strains in Si NWs at elevated temperatures. Overall, Figure 2 and Figures S2–S4 reveal that the Si NWs under tension are brittle at RT but exhibit pronounced plastic deformation followed by fracture at elevated temperatures (e.g., 600 K).

We found that a decrease in the NW diameter can lead to enhanced plastic deformation. Figure 2b also includes the tensile stress–strain curve of a thinner Si NW with a diameter of 24 nm at 600 K, which is qualitatively similar to the Si NW with a diameter of 66 nm at 600 K. However, in this thinner NW, a lower maximum stress of 5.1 GPa was attained at a smaller critical strain of 4.3%, signifying a stronger tendency to plastic deformation. Moreover, the subsequent softening response was sustained over a strain range of 1.6% until the fracture strain ϵ_f of 5.9%; this strain range is defined as plastic strain ϵ_p . Hence, both ϵ_p and ϵ_f measured for the thinner Si NW are larger than the corresponding ϵ_p of 0.7% and ϵ_f of 4.7% for the thicker Si NW (Figure 2b). The more extensive plasticity in the thinner Si NW was manifested by the formation of a number of deformation bands that are uniformly distributed throughout the entire NW (Figure 3a,b), which contrasts with fewer deformation bands in the thicker NW (Figure 2c).

We performed in situ high-resolution TEM (HRTEM) imaging to characterize the deformation bands in the Si NW with a diameter of 24 nm at 600 K. As shown in Figure 3d (corresponding to the boxed area in Figure 3b), the deformation bands first initiated from the free surface (marked by arrows for both twin variants) and then propagated along the inclined plane close to $\{100\}$ in the direction close to $\langle 110 \rangle$. Further growth of these deformation bands were obstructed by the twin boundary. However, an increase of applied load resulted in the transmission of the obstructed deformation bands across the twin boundary, leaving behind twin boundary steps with height of

several atomic layers. Interestingly, the transmitted deformation bands propagated along the inclined plane close to $\{111\}$ in the direction close to $\langle 112 \rangle$. Figure 3d further reveals the atomic structures within the deformation bands, which consist of $1/2\langle 110 \rangle\{001\}$ dislocations, disordered regions (marked by a solid oval), and reoriented grains (marked by dashed square B). The disordered structures can evolve into a new Si phase with the diamond hexagonal (dh) lattice structure (marked by solid square A), which is a 2H polytype of diamond cubic Si with the stacking sequence $\cdots AaBbAaBb \cdots$ along the $\langle 111 \rangle$ direction (known as wurtzite Si⁴³). Both the reoriented grains and new Si phases were verified by selected area diffraction maps in Figure 3c.

Our in situ HRTEM experiments at elevated temperatures indicated that the formation of deformation bands originates from the dominant operation of $1/2\langle 110 \rangle\{001\}$ full dislocations, which were observed in all Si NWs tested at elevated temperatures, irrespective of existence of a central twin boundary (see testing of single crystalline Si in Figure S6 and atomistic simulations showing the effect of twin boundary in Figure S11). This stands in contrast with the dominant activities of $1/2\langle 110 \rangle\{111\}$ full dislocations or $1/6\langle 112 \rangle\{111\}$ partials during plastic deformation of bulk Si structures.⁴⁴ Interestingly, the HRTEM image in Figure 3d reveals three parallel deformation bands at different stages, which clearly reveal the impact of the $1/2\langle 110 \rangle\{100\}$ dislocations. The three stages correspond to the band formation (stage I), growth (stage II), and crossing through the twin boundary (stage III), as schematically illustrated in Figure 3e. During stage I, $1/2\langle 110 \rangle\{001\}$ dislocations nucleate from the NW surface and propagate into the upper twin variant. Gliding of $1/2\langle 110 \rangle\{001\}$ dislocations led to band extension, while climbing of $1/2\langle 110 \rangle\{001\}$ dislocations appears necessary for band

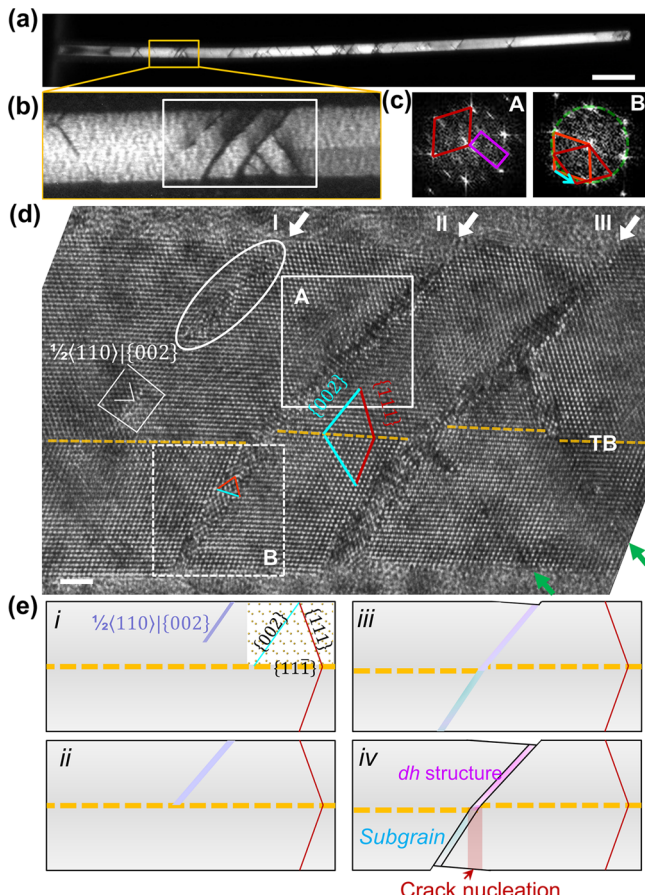


Figure 3. In situ observation of deformation bands and dislocations in a Si NW with a diameter of 24 nm at 600 K. (a,b) Dark-field TEM images showing a number of deformation bands formed in the NW during tensile deformation. Scale bar in (a), 200 nm. (c) FFT filtered diffraction patterns corresponding to the marked regions A and B in (d), showing a *dh* structure and a reoriented grain (39°), respectively. (d) HRTEM observation showing three stages (marked by I–III) of the formation of deformation bands in the boxed area in (b). Disordered structure in stage I is marked by a solid oval. Green arrows indicate the deformation bands initiated from the lower twin variant. Scale bar, 2 nm. (e) Schematic illustration of formation and growth of a deformation band, leading to crack nucleation and fracture in the twinned Si NW.

thickening, accompanied by a slight deviation of band orientation from the {100} plane (Figure 3d,e-ii). These results provide direct evidence that the orientation of deformation bands is dictated by the slip-plane orientation of 1/2<(110)>{001} dislocations. In addition, a variety of plastic deformation processes, including formation of disordered structures, grain reorientation, and transition to the *dh* phase, were observed in these deformation bands (Figure 3d, e-iii). Finally, the transmitted deformation band intersected with the NW surface and also interacted with the nearby deformation band, thus generating large local distortions responsible for surface crack nucleation. After crossing the twin boundary, the surface-initiated crack propagated nearly perpendicular to the twin boundary (Figure 3e-iv) and then grew along the {111} cleavage plane (Figure 2b). Crack growth was accompanied by localized plastic deformation near the crack surface. This kind of dislocation-mediated failure was frequently observed during in situ testing of Si NWs at elevated temperatures (Figure S5).

To understand the critical role of 1/2<(110)>{001} dislocations in the plastic deformation of Si NWs at elevated temperatures, we performed atomistic modeling of surface dislocation nucleation in the <112>-oriented Si NW. To overcome the time scale limitation of molecular dynamics simulation, we used the free-end nudged elastic band (FENE-B) method⁴¹ to calculate energy barriers that control the stress-assisted, thermally activated processes of dislocation nucleation (Supporting Information). We focused on the competing modes of surface nucleation of a 1/2<(110)>{001} loop (Figure 4a) and a 1/2<(110)>{111} loop (Figure 4b). According to transition state theory, to achieve a reasonable frequency (e.g., 1/s) of dislocation nucleation relevant to laboratory experiments, the energy barrier should be on the order of 25 $k_B T$ (where k_B is Boltzmann's constant and T is the absolute temperature),⁴⁵ which is about 0.6 eV at RT and 1.2 eV at 600 K, respectively. These characteristic energy barriers were used to determine whether a dislocation mode would be active at a given temperature. It should be noted that the energy landscape of dislocations in covalently bonded Si often involves both the primary and secondary energy barriers, the latter of which are superimposed on the former.^{6,44} Physically, the primary energy barrier arises from several contributions associated with nucleation of a surface dislocation loop, including the increasing dislocation line energy, the increasing surface ledge energy, and the decreasing mechanical energy due to work done by applied shear stress on dislocation slip. In covalent Si, the secondary energy barriers to dislocation glide can be substantial,^{6,44} such that expansion of a nucleating loop has to overcome a series of secondary barriers associated with local Si bond breaking and switching. Increasing the applied stress usually has a pronounced effect on reducing primary barriers, but is less effective on reducing secondary barriers.

From FENE-B calculations, we obtained the minimum energy path (MEP)⁴⁰ of surface nucleation of a 1/2<(110)>{001} loop (Figure 4c,d), when the Si NW is subjected to an applied tensile stress of 13.2 GPa. It is seen that the MEP is substantially leaned forward due to the high stress applied, indicating the vanishing primary nucleation barrier on an envelope curve (not drawn) connecting local minima. Moreover, this MEP is highly rugged, featuring a series of small secondary barriers on the order of 1–1.2 eV. These secondary barriers can lead to sluggish dislocation motion at RT according to the aforementioned 25 $k_B T$ rule, thus effectively suppressing the nucleation of the 1/2<(110)>{001} dislocations at RT. However, the dislocation mobility can be markedly increased, as the temperature is elevated to 600 K. This is because an increase of thermal energy enables the frequent crossing of energy barriers on the order of about 1.2 eV, thereby promoting the surface nucleation and migration of the 1/2<(110)>{001} dislocations in strained Si NWs, as observed during our in situ TEM experiments. In contrast, Figure 4e,f shows the MEP of surface nucleation of a 1/2<(110)>{111} loop, which was also obtained under the applied tensile stress of 13.2 GPa. This smooth MEP only exhibits a single primary energy barrier with a high value of 4.87 eV. Hence the surface nucleation of 1/2<(110)>{111} dislocations is less favorable than 1/2<(110)>{001} dislocations in <112>-oriented Si NWs under tension at elevated temperatures. The higher primary barrier of surface nucleation of the 1/2<(110)>{111} loop can be partly attributed to the relatively small Schmid factor of 0.41 under axial loading, as opposed to 0.47 for the 1/2<(110)>{001} loop. In addition, differences in surface ledge energy and dislocation line tension can also affect the primary energy barriers for the two competing

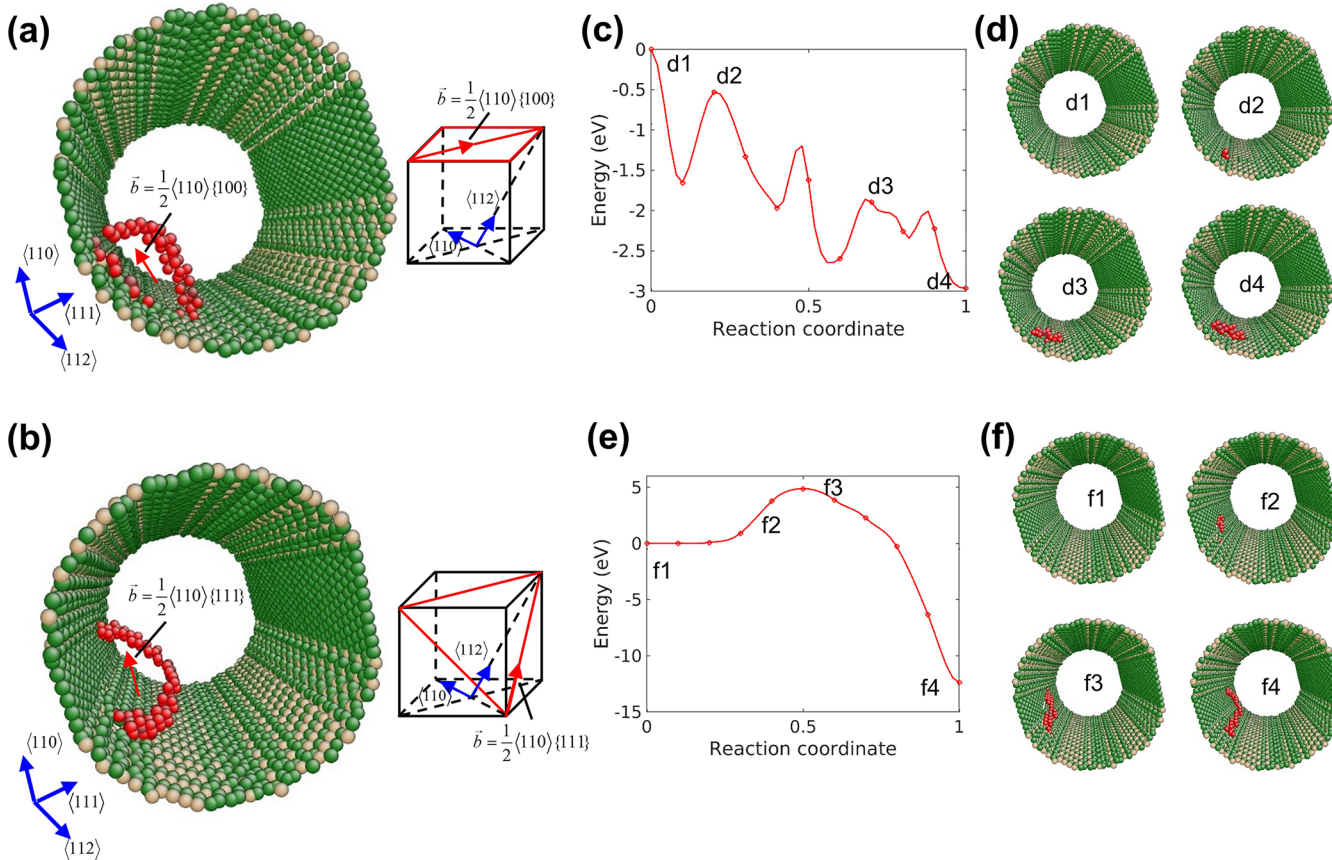


Figure 4. Atomistic reaction pathway modeling results of surface nucleation of a $1/2\langle 110 \rangle\{001\}$ versus a $1/2\langle 110 \rangle\{111\}$ dislocation in a $\langle 112 \rangle$ -oriented Si NW from FENE calculations. (a,b) Atomic configuration showing a fully nucleated $1/2\langle 110 \rangle\{001\}$ and $1/2\langle 110 \rangle\{111\}$ dislocation loop from the side surface of Si NW, respectively. (c) MEP of surface nucleation of a $1/2\langle 110 \rangle\{001\}$ dislocation; (d) corresponding atomic configurations along the MEP, as marked in (c). (e) MEP of surface nucleation of a $1/2\langle 110 \rangle\{111\}$ dislocation, (f1–f4) corresponding atomic configurations along the MEP, as marked in (e). Atoms are colored according to coordination number, so as to display atoms on the NW surface and in the dislocation core. The reaction coordinate in (c,e) is defined as the normalized path length along the MEP.

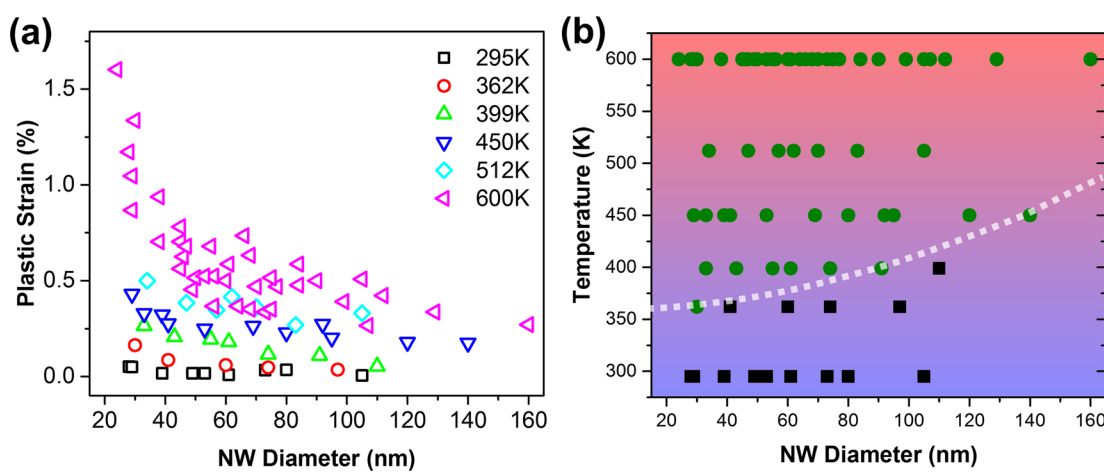


Figure 5. Size and temperature dependence of brittle versus ductile behaviors of 78 Si NWs tested in the temperature range of 295 to 600 K. (a) Measured plastic strain ϵ_p as a function of NW diameter at different temperatures. (b) BDT map in the parameter space of temperature and NW diameter. The ductile NWs ($\epsilon_p > 0.1\%$) are marked by green solid circles, whereas the brittle ones by black solid squares.

dislocation modes. It should be noted that the lack of (or substantially weaker) secondary barriers for nucleation of a $1/2\langle 110 \rangle\{111\}$ loop can be attributed to the close-packed {111} slip planes in diamond cubic Si, which facilitate dislocation glide by eliminating (or largely reducing) the secondary barriers at high loads. Hence, $1/2\langle 110 \rangle\{111\}$ dislocations could become

active at RT, when the primary energy barrier is sufficiently reduced by increasing load (Figure S10), provided that the tensile stress component on the potential cleavage planes is sufficiently low for averting brittle fracture.

To further understand the size and temperature dependence of dislocation-mediated plasticity and fracture, we tested 78 Si

NWs with the diameter range of 24–160 nm and in the temperature range of 295–600 K. As shown in Figure 5a, the plastic strain ϵ_p increases with decreasing NW diameter. For example, at 600 K ϵ_p increases from 0.27 to 1.6%, as the NW diameter decreases from 160 to 24 nm. For the same diameter, ϵ_p increases with temperature. The results of the 78 Si NWs tested are summarized in a deformation mechanism map of Figure 5b. In this map, green circles represent Si NWs with dislocation-mediated failure, whereas black squares Si NWs with brittle cleavage fracture. A transition line, as defined by a critical ϵ_p of 0.1%, is drawn to separate the regimes of brittle and dislocation-mediated responses. The map also reveals that as the NW diameter decreases, the critical temperature associated with dislocation-mediated plastic deformation decreases. For example, the Si NW with diameter of 110 nm showed brittle fracture at 398 K, while the NW with diameter of 30 nm exhibited plastic deformation with dislocation activities even at 362 K (Figure S8). Hence, Figure 5b indicates that both the increase of temperature and the decrease of NW diameter can promote plastic deformation in Si NWs, leading to dislocation-mediated failure (Figures S7–S9).

Discussions. Plastic deformation with extensive dislocation activities is critical for the BDT in both bulk and nanoscale Si crystals. Full dislocations of $1/2\langle 110 \rangle\{111\}$, which can dissociate into $1/6\langle 112 \rangle\{111\}$ partials, are responsible for most of the reported plastic deformation in bulk Si crystals,^{44,46} similar to face-centered cubic metals.^{47–49} Dislocation activities on $\{111\}$ slip planes have also been reported in Si nanostructures (such as nanocubes and nanopillars) under compression at RT to serve as experimental evidence of size-dependent BDT.^{21,50} Overall, the onset of plastic deformation, including activities of dislocation nucleation and propagation, in Si crystals is deemed to have a strong dependence on loading condition, stress state, strain rate, temperature, and sample size.^{21,27,44,50–52} In this study, we focused on the uniaxial tension of Si NWs but we did not observe any twinning during plastic deformation between 300 and 600 K. This can be well related to the lack of $1/6\langle 112 \rangle\{111\}$ partials in the present experimental conditions. We showed that the unconventional $1/2\langle 110 \rangle\{001\}$ dislocations can become highly active in $\langle 112 \rangle$ -oriented Si NWs at elevated temperatures. This is attributed to the following possible factors: the high Schmid factor (0.47) that favors the $1/2\langle 110 \rangle\{001\}$ slip system (see Table S1), the high stress attainable in Si NWs, and the assistance of elevated temperatures for overcoming the secondary energy barriers of $1/2\langle 110 \rangle\{001\}$ dislocation glide.

In bulk Si, the BDT typically involves a transition from cleavage fracture to extensive plastic deformation that might end up with ductile tearing.^{9,10} In contrast, what we observed from Si NWs at elevated temperatures is the initial ductile response associated with dislocation plasticity (as evidenced by the necking deformation in Figure 2b and Figures S4 and S7–S9) followed by “brittle fracture” (i.e., cracks grew along the cleavage planes), at least for the temperature and NW diameter ranges studied in this work. These results represent a BDT mode in Si NWs different from that in bulk Si, which arises presumably due to the small volume, large surface area, and high stress associated with Si NWs that collectively limit the extent of plastic deformation before the tensile failure of Si NWs. Taking into account the size effect, the transition temperature for BDT might go over 600 K as the NW diameter increases to hundreds of nanometer. In addition to sample size, the BDT temperature would depend on crystal orientation, microstructure, loading

mode (tension, compression, or bending), with or without precracks, and so forth.

The twin boundary in the center of the Si NW plays an important role in obstructing the propagation of both individual dislocations (Figure S11) and deformation bands. This obstruction will result in back stresses that impede the continued operation of the same surface dislocation sources. As a result, plastic deformation becomes delocalized, an effect known to enhance the tensile ductility. As the NW diameter is reduced, the thickness of the twin variant is decreased. Hence the twin boundary can further promote the delocalized plastic deformation, thereby enhancing the tensile ductility, as shown in Figure 5. This reinforces the notion of harnessing internal interfaces for enhancing the tensile ductility of nanostructured materials.^{53–55}

Finally, we note the formidable role that quantitative in situ nanomechanical testing at elevated temperatures can play in our understanding of the nano-thermomechanical behavior of materials. Not only can they provide quantitative characterization and critical insight for the brittle and ductile responses of Si nanostructures but also can be extended for other studies of mechanical behavior of nanoscale materials at elevated temperatures.

Materials and Methods. Sample Synthesis and Characterization. Si NWs were synthesized by chemical vapor deposition (CVD) using gold nanoclusters as catalysts and silane (SiH_4) as a vapor-phase reactant, following the method developed by Wu et al.⁵⁶ Gold nanoclusters with diameters ranging from 10 to 50 nm were deposited on Si substrates capped with a 600 nm thick layer of thermal silicon dioxide. The substrates were placed in a quartz tube furnace (EasyTube 3000, First Nano). After a 30 min purge in H_2 ambient at 50 Torr, VLS growth of Si NWs was carried out at 480 °C, 15 Torr for 10 min with the flow of SiH_4 (20 sccm) and H_2 (200 sccm).

High-resolution TEM observations were performed on JEOL 2010F with a Schottky field emission gun (FEG) operated at 200 kV.

In Situ SEM/TEM Mechanical Testing. The mechanical testing was carried out in situ inside a TEM using a MEMS-based material testing stage, which consists of an electrostatic (comb-drive) actuator, a capacitive load sensor and an on-chip heater (Figure S1a). The stage was fabricated out of one layer of single crystalline silicon with thickness of 25 μm . The on-chip heater is based on Joule heating of the single crystalline silicon structure itself (i.e., no additional heating layer) (Figure S1b). The temperature (from RT to 600 K) on the sample area is controllable by changing the applied voltage on the on-chip heater. A key feature of this testing stage is the symmetry of the overall structure (i.e., the electrostatic actuator and the capacitive load sensor are identical). Details on the testing stage has been reported previously.³⁸

The temperature is uniformly distributed along the Si NW, which was verified by the Raman spectroscopy measurement. Figure S1c shows the Stokes-shifted Raman spectra of the gap edge of the device (dark line) and the middle of a Si NW (red line) under 8 V heating voltage in air, respectively. Note that the NW is clamped across a gap between the actuator and the load sensor. The difference in temperature between the two locations was less than 2 K. The peak shift in Figure S1c reflects the temperature change following a linear relationship.³⁸ The large difference in the spectra amplitude is because the probe areas in the middle of the Si NW is much smaller than that in the gap edge of the device.

Si NWs were mounted on the testing stage using a nanomanipulator (Klocke Nanotechnik, Germany) inside a FEI Quanta 3D FEG dual beam. An individual Si NW was welded to the nanomanipulator probe, then mounted to the MEMS stage and clamped by electron-beam-induced Pt deposition at the two free ends. Two local markers were deposited on the NWs for displacement (and strain) measurement. Displacement (and strain) is measured by digital image correlation of TEM images of two local markers on the specimen (Figure S1d), giving rise to a strain resolution of 0.01% (gage length 2 μ m). The stress resolution depends on the NW diameter (e.g., 1.4 MPa for a NW diameter of 104 nm⁵⁷). In situ TEM mechanical testing was performed in JEOL 2010F. The loading and unloading strain rates were \sim 0.003%/s. Low-magnification images were recorded at a fixed condense (the second condense lens) current to minimize the focus change. The current density of incident e-beam was <0.1 A/cm² and its effect on the mechanical behavior of the NWs under tensile testing can be neglected.

Atomistic Modeling. The free-end nudged elastic band (FENE⁴¹) calculation is performed using the Stillinger–Weber (SW) Si potential¹⁸ with an in-house code. The {112}-oriented Si NW has a circular cross section with the diameter of \sim 9 nm. It contains 39 616 Si atoms. The periodic boundary condition is applied along the axial direction of the Si NW. The lateral side of the NW is freely relaxed. After relaxation by conjugate gradient energy minimization, the supercell along the NW direction has a length of 10.6 nm. Following a similar dislocation embedding scheme in our previous study,^{59,60} a surface dislocation loop in the NW is created by the following operations using LAMMPS: (i) define a surface dislocation loop by selecting a patch of Si atoms on the two adjacent {111} or {100} planes; (ii) impose a relative shear displacement of $a_0/2$ ⟨110⟩ (where a_0 is the lattice constant) between the two layers of atoms in the patch; specifically, the shear displacement is increased incrementally in 10 steps and the atomic structure is partially relaxed after shearing in each step while holding the atoms in the patch fixed; (iii) partially relax the entire NW to obtain a sufficiently large dislocation loop that can be used as the free-end state of the FENE⁴¹ calculation.

ASSOCIATED CONTENT

Supporting Information

The Supporting Information is available free of charge on the ACS Publications website at DOI: [10.1021/acs.nanolett.9b01789](https://doi.org/10.1021/acs.nanolett.9b01789).

Description of MEMS device, post-mortem characterization of the fracture morphology, in situ mechanical testing of Si NWs at 362, 399, and 450 K, atomistic reaction pathway modeling results and molecular statics simulation snapshots, Schmid factors of typical slip systems in Si (PDF)

Mechanical response and microstructure evolution of a Si NW with diameter of 61 nm (corresponding to the one in Figure 2a) under in situ TEM tensile testing at room temperature; NW shows brittle fracture (AVI)

Mechanical response and microstructure evolution of a Si NW with diameter of 66 nm (corresponding to the one in Figure 2b) under in situ TEM tensile testing at 600 K; NW shows dislocation-mediated plastic deformation followed by fracture (AVI)

AUTHOR INFORMATION

Corresponding Authors

*E-mail: ting.zhu@me.gatech.edu.
*E-mail: yong_zhu@ncsu.edu.

ORCID

Guangming Cheng: [0000-0001-5852-1341](https://orcid.org/0000-0001-5852-1341)

Yong Zhu: [0000-0002-3862-5757](https://orcid.org/0000-0002-3862-5757)

Notes

The authors declare no competing financial interest.

ACKNOWLEDGMENTS

We acknowledge financial support from the National Science Foundation (NSF) under Award No. CMMI-1762511. We also acknowledge the use of the Analytical Instrumentation Facility (AIF) at North Carolina State University, which is supported by the State of North Carolina and the National Science Foundation (award number ECCS-1542015). The AIF is a member of the North Carolina Research Triangle Nanotechnology Network (RTNN), a site in the National Nanotechnology Coordinated Infrastructure (NNCI).

REFERENCES

- Hochbaum, A. I.; Chen, R.; Delgado, R. D.; Liang, W.; Garnett, E. C.; Najarian, M.; Majumdar, A.; Yang, P. *Nature* **2008**, *451* (7175), 163–167.
- Chan, C. K.; Peng, H.; Liu, G.; McIlwrath, K.; Zhang, X. F.; Huggins, R. A.; Cui, Y. *Nat. Nanotechnol.* **2008**, *3* (1), 31–35.
- Xu, F.; Lu, W.; Zhu, Y. *ACS Nano* **2011**, *5* (1), 672–678.
- Takei, K.; Takahashi, T.; Ho, J. C.; Ko, H.; Gillies, A. G.; Leu, P. W.; Fearing, R. S.; Javey, A. *Nat. Mater.* **2010**, *9* (10), 821–826.
- Zheng, G.; Patolsky, F.; Cui, Y.; Wang, W. U.; Lieber, C. M. *Nat. Biotechnol.* **2005**, *23* (10), 1294.
- Argon, A. S. *J. Eng. Mater. Technol.* **2001**, *123* (1), 1–11.
- Samuels, J.; Roberts, S. *Proc. R. Soc. London, Ser. A* **1989**, *421* (1860), 1–23.
- Ostlund, F.; Rzepiejewska-Malyska, K.; Leifer, K.; Hale, L. M.; Tang, Y.; Ballarini, R.; Gerberich, W. W.; Michler, J. *Adv. Funct. Mater.* **2009**, *19* (15), 2439–2444.
- Nakao, S.; Ando, T.; Shikida, M.; Sato, K. *J. Micromech. Microeng.* **2008**, *18* (1), 015026.
- Jaya, B. N.; Wheeler, J. M.; Wehrs, J.; Best, J. P.; Soler, R.; Michler, J.; Kirchlechner, C.; Dehm, G. *Nano Lett.* **2016**, *16* (12), 7597–7603.
- Brede, M. *Acta Metall. Mater.* **1993**, *41* (1), 211–228.
- Hirsch, P.; Roberts, S. *Philos. Mag. A* **1991**, *64* (1), 55–80.
- Hintsala, E. D.; Gerberich, W. W. *Mater.* **2018**, *4*, 175–181.
- Hintsala, E. D.; Bhowmick, S.; Yueyue, X.; Ballarini, R.; Asif, S. S.; Gerberich, W. W. *Scr. Mater.* **2017**, *130*, 78–82.
- Teresi, C. S.; Gerberich, W. W. *Scr. Mater.* **2018**, *144*, 56–59.
- Scandian, C.; Azzouzi, H.; Maloufi, N.; Michot, G.; George, A. *physica status solidi (a)* **1999**, *171* (1), 67–82.
- Nakao, S.; Ando, T.; Shikida, M.; Sato, K. *J. Micromech. Microeng.* **2006**, *16* (4), 715.
- Gerberich, W. W.; Stauffer, D. D.; Beaber, A. R.; Tymiak, N. I. *J. Mater. Res.* **2012**, *27* (3), 552–561.
- Hirsch, P.; Roberts, S. *Acta Mater.* **1996**, *44* (6), 2361–2371.
- Chrobak, D.; Tymiak, N.; Beaber, A.; Ugurlu, O.; Gerberich, W. W.; Nowak, R. *Nat. Nanotechnol.* **2011**, *6* (8), 480–484.
- Merabet, A.; Texier, M.; Tromas, C.; Brochard, S.; Pizzagalli, L.; Thilly, L.; Rabier, J.; Talneau, A.; Le Vaillant, Y. M.; Thomas, O.; Godet, J. *Acta Mater.* **2018**, *161*, 54–60.
- Han, X.; Zheng, K.; Zhang, Y.; Zhang, X.; Zhang, Z.; Wang, Z. L. *Adv. Mater.* **2007**, *19* (16), 2112–2118.
- Kizuka, T.; Takatani, Y.; Asaka, K.; Yoshizaki, R. *Phys. Rev. B: Condens. Matter Mater. Phys.* **2005**, *72* (3), 035333.

(24) He, Y.; Zhong, L.; Fan, F.; Wang, C.; Zhu, T.; Mao, S. X. *Nat. Nanotechnol.* **2016**, *11* (10), 866–871.

(25) Zheng, K.; Han, X.; Wang, L.; Zhang, Y.; Yue, Y.; Qin, Y.; Zhang, X.; Zhang, Z. *Nano Lett.* **2009**, *9* (6), 2471–2476.

(26) Wang, L.; Zheng, K.; Zhang, Z.; Han, X. *Nano Lett.* **2011**, *11* (6), 2382–2385.

(27) Tang, D.-M.; Ren, C.-L.; Wang, M.-S.; Wei, X.; Kawamoto, N.; Liu, C.; Bando, Y.; Mitome, M.; Fukata, N.; Golberg, D. *Nano Lett.* **2012**, *12* (4), 1898–1904.

(28) Kang, W.; Saif, M. T. A. *Adv. Funct. Mater.* **2013**, *23* (6), 713–719.

(29) Zhu, Y.; Xu, F.; Qin, Q.; Fung, W. Y.; Lu, W. *Nano Lett.* **2009**, *9* (11), 3934–3939.

(30) Hoffmann, S.; Utke, I.; Moser, B.; Michler, J.; Christiansen, S. H.; Schmidt, V.; Senz, S.; Werner, P.; Gösele, U.; Ballif, C. *Nano Lett.* **2006**, *6* (4), 622–625.

(31) Gordon, M. J.; Baron, T.; Dhalluin, F.; Gentile, P.; Ferret, P. *Nano Lett.* **2009**, *9* (2), 525–529.

(32) Kim, Y. J.; Son, K.; Choi, I. C.; Choi, I. S.; Park, W. I.; Jang, J. i. *Adv. Funct. Mater.* **2011**, *21* (2), 279–286.

(33) Steighner, M.; Snedeker, L.; Boyce, B.; Gall, K.; Miller, D.; Muhlstein, C. *J. Appl. Phys.* **2011**, *109* (3), 033503.

(34) Greer, J. R.; Oliver, W. C.; Nix, W. D. *Acta Mater.* **2005**, *53* (6), 1821–1830.

(35) Uchic, M. D.; Dimiduk, D. M.; Florando, J. N.; Nix, W. D. *Science* **2004**, *305* (5686), 986–989.

(36) Wang, L.; Teng, J.; Sha, X.; Zou, J.; Zhang, Z.; Han, X. *Nano Lett.* **2017**, *17* (8), 4733–4739.

(37) Zhu, Y.; Espinosa, H. D. *Proc. Natl. Acad. Sci. U. S. A.* **2005**, *102* (41), 14503–14508.

(38) Chang, T.-H.; Zhu, Y. *Appl. Phys. Lett.* **2013**, *103* (26), 263114.

(39) Zhu, Y.; Moldovan, N.; Espinosa, H. D. *Appl. Phys. Lett.* **2005**, *86* (1), 013506.

(40) Jonsson, H., G., Mills, K. W., Jacobsen In *Classical and Quantum Dynamics in Condensed Phase Simulations*; Berne, B. J., Ciccotti, G., Coker, D. F., Eds.; World Scientific, 1998; pp 385–404.

(41) Zhu, T.; Li, J.; Samanta, A.; Kim, H. G.; Suresh, S. *Proc. Natl. Acad. Sci. U. S. A.* **2007**, *104*, 3031–3036.

(42) Cook, R. F. *J. Mater. Sci.* **2006**, *41* (3), 841–872.

(43) Kasper, J.; Wentorf, R. *Science* **1977**, *197* (4303), 599.

(44) Cai, W.; Bulatov, V. V.; Chang, J. P.; Li, J.; Yip, S. Dislocation Core Effects on Mobility. In *Dislocations in Solids*; Nabarro, F. R. N., Hirth, J. P., Eds.; Elsevier: Amsterdam, 2004; Vol. 12, pp 1–80.

(45) Cottrell, A. H. *Philos. Mag.* **2006**, *86* (25–26), 3811–3817.

(46) Rabier, J.; Pizzagalli, L.; Demenet, J. *Dislocations in solids* **2010**, *16*, 47–108.

(47) Wang, L.; Han, X.; Liu, P.; Yue, Y.; Zhang, Z.; Ma, E. *Phys. Rev. Lett.* **2010**, *105* (13), 135501.

(48) Wang, L.; Guan, P.; Teng, J.; Liu, P.; Chen, D.; Xie, W.; Kong, D.; Zhang, S.; Zhu, T.; Zhang, Z.; et al. *Nat. Commun.* **2017**, *8* (1), 2142.

(49) Cheng, G. M.; Yin, S.; Chang, T. H.; Richter, G.; Gao, H. J.; Zhu, Y. *Phys. Rev. Lett.* **2017**, *119* (25), 256101.

(50) Wagner, A. J.; Hintsala, E. D.; Kumar, P.; Gerberich, W. W.; Mkhoyan, K. A. *Acta Mater.* **2015**, *100*, 256–265.

(51) El Nabi, F. A.; Godet, J.; Brochard, S.; Pizzagalli, L. *Modell. Simul. Mater. Sci. Eng.* **2015**, *23* (2), 025010.

(52) Korte, S.; Clegg, W. *Scr. Mater.* **2009**, *60* (9), 807–810.

(53) Lu, K.; Lu, L.; Suresh, S. *Science* **2009**, *324* (5925), 349–352.

(54) Zhu, T.; Li, J. *Prog. Mater. Sci.* **2010**, *55*, 710–757.

(55) Narayanan, S.; Cheng, G.; Zeng, Z.; Zhu, Y.; Zhu, T. *Nano Lett.* **2015**, *15* (6), 4037–4044.

(56) Wu, Y.; Cui, Y.; Huynh, L.; Barrelet, C. J.; Bell, D. C.; Lieber, C. M. *Nano Lett.* **2004**, *4* (3), 433–436.

(57) Qin, Q.; Yin, S.; Cheng, G.; Li, X.; Chang, T.-H.; Richter, G.; Zhu, Y.; Gao, H. *Nat. Commun.* **2015**, *6*, 5983.

(58) Stillinger, F. H.; Weber, T. A. *Phys. Rev. B: Condens. Matter Mater. Phys.* **1985**, *31* (8), 5262–5271.

(59) Chen, D.; Costello, L. L.; Geller, C. B.; Zhu, T.; McDowell, D. L. *Acta Mater.* **2019**, *168*, 436–447.

(60) Kacher, J.; Zhu, T.; Pierron, O.; Spearot, D. E. *Curr. Opin. Solid State Mater. Sci.* **2019**, *23* (3), 117–128.